Trade-off between second- and third-order nonlinearities, ultrafast free carrier absorption and material damage in silicon nanoparticles

Anton Rudenko Aoxue Han Jerome V. Moloney*

Arizona Center for Mathematical Sciences and Wyant College of Optical Sciences, University of Arizona, Tucson, Arizona 85721, USA
Email Address: antmipt@gmail.com

Keywords: *Ultrashort laser, Harmonic generation, Silicon photonics, Mie resonance, Lattice resonance, Free carrier absorption, Material Damage*

Reaching the optimal second- and third-order nonlinear conversion efficiencies while avoiding undesirable free carrier absorption losses and material damage in ultrashort laser-excited nanostructures is a challenging obstacle in all-dielectric ultrafast nanophotonics. In order to elucidate the main aspects of this problem, we develop a multi-physical model, coupling nonlinear Maxwell equations supplied by surface and bulk nonlinearities with free carrier hydrodynamic equations for electron-hole plasma kinetics and electron-ion transfer for silicon. We compare the maximum feasible efficiencies for a single spherical particle supporting different electric and magnetic resonances and propose to further optimize the harmonic yield by implementing lattice resonances in a periodic arrangement of nanoparticles. Results support the dominant role of magnetic dipole and quadrupole contributions in the enhancement of the third harmonic and the electric dipole for the second harmonic, as well as the possibility to further improve the conversion of both harmonics simultaneously at least by two orders of magnitude by designing properly the resonant metasurface.

1 Introduction

All-dielectric nanostructures, supporting individual Mie or collective resonances, can boost harmonic generation up to record conversion efficiencies in ultrashort laser-matter interactions [1–8]. One of the crucial advantages is a relatively high damage threshold of such materials, in comparison with plasmonic counterparts or unstructured samples. Nevertheless, the limitations due to free carrier absorption losses and material damage are still relevant in pursuit of the optimal laser parameters and geometries for record harmonic enhancement and while paving the way from perturbative to non-perturbative regimes in nonlinear optics.

A theoretical framework to describe the perturbative excitation of nanostructures and low-order harmonic generation has been developed over the last few decades [9–16]. It was established that different mechanisms are involved in SHG from non-centrosymmetric and centrosymmetric semiconductor materials. The latter ones inherit the inversion symmetry that forbids an electric dipole second-order susceptibility. Nevertheless, the symmetry is broken by bulk quadrupole and surface dipole contributions [17, 18]. In order to describe the nonlinear optical response of centrosymmetric materials such as silicon (Si), a phenomenological model was proposed by Bloembergen et al. [9] and applied to specific nanostructures in the recent studies [3, 19]. In the pioneering work [9], the correspondence between phenomenological and a hydrodynamic model for free electrons, commonly applied to describe second-order nonlinear response from metals [13], was demonstrated. These two approaches, originally designed for bound and free electrons and coupled to Maxwell equations by the nonlinear polarization, form the basis to describe the perturbative nonlinear response of arbitrary nanostructures.

Upon ultrashort laser excitation of all-dielectric materials, optical properties swiftly change due to photoionization processes, while free carrier absorption may lead to the local material damage. On the one hand, these effects are commonly considered as the limiting factors for the operating frequency conversion nanodevices [1, 2, 20–23]. On the other hand, inhomogeneous free carriers can serve as an additional source for symmetry breaking [24,25] and for high-order harmonics generation in non-perturbative regimes [7, 8, 26, 27], and participate in ultrafast self-action, all-optical switching and modulation at the nanoscale [20, 28–32]. While the applicability of the perturbative approaches is limited to describe weak intensity regimes, the extended hydrodynamic model for electron-hole plasma kinetics and electron-ion transfer gives a reliable estimate for the inhomogeneous absorption and heating processes inside the laser-excited

nanostructures and describes the non-perturbative mechanism of harmonic generation due to direct electron transitions from valence to conduction band. To date, a self-consistent approach, considering both nonlinear sources and laser-induced electron-hole dynamics has not been proposed and applied in the context of SHG and THG.

In the current work, a multi-physical approach is developed in order to explore the natural material limitations for nonlinear conversion efficiency achievable by ultrashort laser irradiation of Si nanoparticles (NPs) below the melting point. Nonlinear propagation, dynamic build-up of free carriers, and harmonic generation are modeled in a self-consistent way and compared for a wide range of resonant and off-resonant conditions. Based on the results for a single NP, further step forward is done by coupling electric and magnetic dipole resonances in an infinite array of NPs to enhance both second- and third-order harmonic yield.

2 Model details

To model nonlinear propagation through a semiconductor nanostructure, we solve the full-vector Maxwell equations with polarization density $\vec{P}$ (corresponding current density $\vec{J} = \frac{\partial \vec{P}}{\partial t}$), incorporating dispersion and perturbative nonlinear contributions relevant for a centrosymmetric material (Si), and current density for free carriers $\vec{J}_e$ as follows

$$\begin{cases} \dfrac{\partial \vec{E}}{\partial t} = \dfrac{\nabla \times \vec{H}}{\epsilon_0} - \dfrac{\vec{J}_e + \vec{J}}{\epsilon_0} \\ \dfrac{\partial \vec{H}}{\partial t} = -\dfrac{\nabla \times \vec{E}}{\mu_0}, \end{cases} \tag{1}$$

where $\vec{E}$ and $\vec{H}$ are the electric and the magnetic fields, ϵ_0 and μ_0 are the permittivity and the permeability of free space.

The electric field source was chosen to be a linearly x-polarized Gaussian pulse with a full width at half maximum of $\theta = 100$ fs and a central wavelength of $\lambda = 800$ nm. Light propagates along the z direction. Spatially, we consider a plane wave, therefore, a single NP or NPs in array are irradiated uniformly. In most of the experiments with nanostructures, the focusing conditions are not extremely tight ($NA \approx 0.4$ or looser) [3, 7, 21], corresponding to the beam's waist from several to tens of microns significantly larger compared to the subwavelength size of the considered NPs. Therefore, the uniformity produced by laser focusing is much less pronounced than the uniformity caused by inhomogeneous field distributions at the nanoscale inside the NPs. In metasurfaces, comprising a finite array of periodically arranged NPs, however, tight focusing conditions may affect the symmetry of the problem and the quality factor of the resonators.

Maxwell equations are solved by the finite-difference time-domain (FDTD) approach with convolutional perfect matched layers (CPML) at the boundaries [33]. The electron current density $\vec{J}_e$ is coupled to Maxwell equations (1) by applying the auxiliary differential equation technique and implementing the nonlinear algorithm described in Ref. [34].

In order to introduce the perturbative polarization response $\vec{P}$, we apply an explicit formulation for second- and third-order optical nonlinearities in the FDTD approach [15]. In case of a centrosymmetric material, the surface contributions to second order are reduced to the components

$$(P_x^{(2)}; P_y^{(2)}; P_z^{(2)}) = (2\chi_{xxz}^{(2)} E_x E_z; 2\chi_{yyz}^{(2)} E_y E_z; \chi_{zzz}^{(2)} E_z^2 + \chi_{zxx}^{(2)} E_x^2 + \chi_{zyy}^{(2)} E_y^2), \tag{2}$$

where $\chi_{zzz}^{(2)} = 65 \cdot 10^{-19}$ m^2/V, $\chi_{xxz}^{(2)} = \chi_{yyz}^{(2)} = 3.5 \cdot 10^{-19}$ m^2/V, and $\chi_{zxx}^{(2)} = \chi_{zyy}^{(2)} = 1.3 \cdot 10^{-19}$ m^2/V measured in Ref. [35]. Additional bulk contributions are due to convection, magnetic Lorentz and quadrupolar terms, linked to β and γ parameters in a phenomenological model proposed by Bloembergen et al. [9]. Here, we use β and γ parameters, measured for Si in Ref. [36], rather than the effective

mass of bound electrons, which is often unknown or used as a fitting parameter in the hydrodynamic formulation [37]. The combined equation then takes the following form

$$\begin{aligned}\frac{\partial^2\vec{P}}{\partial t^2}+\gamma_p\frac{\partial\vec{P}}{\partial t}+\omega_0^2\vec{P}+\frac{\beta^2}{2\gamma}\sum_k\frac{\partial\left(\vec{J}J_k\right)}{\partial r_k}\\ =\omega_p^2\left[\vec{E}+\vec{P}^{(2)}+\chi^{(3)}\vec{E}(\vec{E}\vec{E})+2\beta\mu_0[\vec{J}\times\vec{H}]-2\beta(\vec{E}\nabla\vec{P})\right],\end{aligned} \tag{3}$$

where γ_p, ω_0, ω_p are the damping constant, resonance and plasma frequencies in the Lorentz formulation for Si dispersion at visible and UV wavelengths from Ref. [14], $\chi^{(3)}=4n^2\epsilon_0 cn_2/3\approx 1.9\times10^{-15}$ cm^2/V^2 is the third-order susceptibility at 800 nm [38], where $n=3.6941$ is the corresponding refractive index of Si.

The equations describing the optical response of carriers in the conduction band, the involved photoionization processes and the energy transfer between the electrons and ions are written as follows

$$\begin{cases}\dfrac{\partial\vec{J}_e}{\partial t}=-\vec{J}_e\nu_e+\dfrac{e^2N_e}{m_e^*}\vec{E}\\ \dfrac{\partial N_e}{\partial t}=\dfrac{N_a-N_e}{N_a}\left(\dfrac{\alpha I}{\hbar\omega}+\dfrac{\beta I^2}{2\hbar\omega}+w_{av}N_e\right)+D_e\Delta N_e-\dfrac{C_A{N_e}^3}{C_A\tau_{rec}N_e^2+1}\\ C_e\dfrac{\partial T_e}{\partial t}=\nabla\cdot(k_e\nabla T_e)-\gamma_{ei}(T_e-T_i)+\vec{J}_e\cdot\vec{E}-E_gw_{av}\\ C_i\dfrac{\partial T_i}{\partial t}=\nabla\cdot(k_i\nabla T_i)+\gamma_{ei}(T_e-T_i),\end{cases} \tag{4}$$

where e, N_e and T_e are the electron charge, density and temperature and T_i is the ion temperature, $m_e^*=0.18m_e$ is the reduced electron-hole mass and $\nu_e=10^{15}$ s^{-1} is the electron collision frequency related to the Drude damping time [39]. $I=\frac{\varepsilon_0 c}{2}\left|\vec{E}\right|^2$ is the intensity, $\omega=2\pi c/\lambda$ is the central frequency, $\alpha=1.12\times10^3\exp(T_i/430)$ cm^{-1} and $\beta=9$ cm/GW are the one- and two-photon absorption coefficients, respectively [40], $N_a=5\times10^{22}$ cm^{-3} is the Si atom density, $C_A=3.8\times10^{-31}$ cm^6/s is the Auger recombination rate [40, 41], $\tau_{rec}=6\times10^{-12}$ s is the minimum Auger recombination time [42]. The secondary electrons are produced by the avalanche ionization $w_{av}=3.6\cdot10^{10}\exp(-1.5E_g/k_bT_e)$ s^{-1} [40, 41], where $E_g(N_e,T_i)$ is the electron bandgap of photo-excited Si from Ref. [41]. The equation for free carriers N_e includes the carrier ambipolar diffusion with diffusivity $D_e=5400/T_i$ cm^2/s [40, 41].

The equation for the electron temperature includes electron diffusion, an electron-ion coupling term, Joule heating by Drude absorption $\vec{J}_e\cdot\vec{E}$ and energy losses due to avalanche development E_gw_{av}. The electron heat capacity is approximated by $C_e=3k_BN_e$, where k_B is the Boltzmann constant. The electron heat conductivity $k_e(T_e)$, lattice heat capacity $C_i(T_i)$ and thermal conductivity $k_i(T_i)$ are obtained from Ref. [40]. The electron-ion coupling factor is related to the electron capacity as $\gamma_{ei}=C_e/\tau_{ei}$ with carrier-phonon relaxation time $\tau_{ei}(N_e)$ from Ref. [43].

3 Results and discussion

3.1 Single nanoparticle

We start our analysis by investigating the optical response of a single Si NP, irradiated by a near-infrared femtosecond laser pulse. The extinction cross-sections of a particle as a function of wavelength and sphere radius calculated by Mie theory for a homogeneous Si sphere [44] are shown in Fig. 1(a). In the sub-wavelength range, the NP exhibits a variety of Mie resonances, with a particularly pronounced magnetic dipole and quadrupole resonances. For the laser wavelength of 800 nm, the resonant and off-resonant sizes chosen for this study are indicated in Fig. 1(b). It is worth noting that mainly the resonances of lower order (dipoles, quadrupoles) are of interest because higher modes may require a high number of

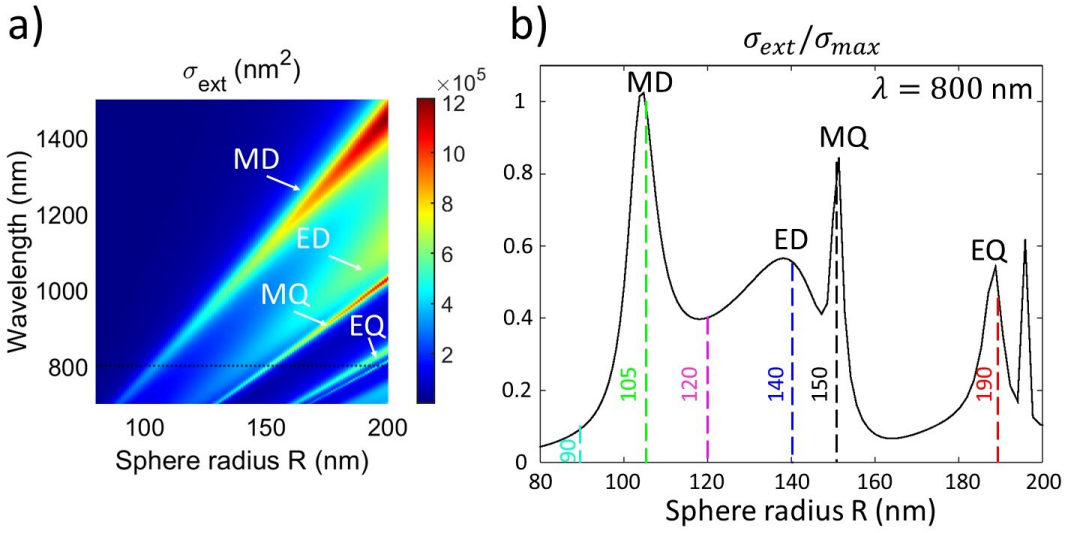

Figure 1: (a) Extinction cross-section as a function of laser wavelength and NP radius. Mie resonances are indicated: magnetic dipole (MD), electric dipole (ED), magnetic quadrupole (MQ), electric quadrupole (EQ). (b) NP radii investigated in the current work and their position in relation to Mie resonances at laser wavelength of $\lambda = 800$ nm. Extinction cross-section are normalized to the maximum value σ_{max} at MD.

optical cycles to be excited [24]. Another interesting aspect is the resonance width which varies for different types of resonances with the broadest one for the electric dipole resonance. One may expect that significantly lower input electric fields compared to off-resonant cases are required to excite magnetic dipole modes but also to reach the damage threshold. In our study, we investigate the nonlinear optical response for NPs of different sizes and different field distributions and enhancement factors approaching the melting threshold for Si (i. e. the energy absorbed by excited electron-hole carriers enough to heat locally the particle up to $T_m \approx 1685$ K). The predicted trends in the current work are independent of the exact threshold value, keeping in mind that irreversible particle reshaping may occur at slightly different temperatures, depending on the polycrystallinity, doping content and heating dynamics of the sample [45], but also via nonthermal way by strong ultrafast carrier excitation [46].
Nonlinear Maxwell simulations coupling Eqs. (1), (3) and (4) are performed for a near-infrared femtosecond laser pulse excitation of a single NP. The input intensities I_0 are chosen then to correspond to the temperature distribution locally reaching the melting threshold inside the NP. In addition to the maximum practicable intensity inside a Si NP, limited by possible material damage, the spatial intensity distribution varies a lot depending on the size parameter. These distributions are plotted in Fig. 2(a-f). Resonant excitation of electric and magnetic dipole and quadrupole modes in subwavelength NPs is at the origin of the intrinsic intensity distribution inhomogeneity. Furthermore, the nonlinear intensity distribution may deviate from the linear one due to the following reasons. Firstly, a finite number of optical cycles in ultrashort pulses and different quality factors of the resonant modes (related to the number of optical cycles required to excite a particular mode) may result in the situation when low-order modes such as electric dipole mode would be excited beforehand, whereas high-order modes would be delayed and less pronounced [24]. Secondly, strong field confinement inside the NP causes inhomogeneous distribution of carriers already before the maximum intensity is reached, which would affect further propagation of the Gaussian pulse (particularly, in case of larger NPs) because the laser-induced plasma would absorb and reflect light more efficiently.
More particularly, the pattern inside the NPs represents a toroidal structure for the sizes below and close to the magnetic dipole (MD) resonance in Fig. 2(a,b), single spot distributions close to electric dipole (ED) resonance in Fig. 2(c,d), and complex patterns for magnetic and electric quadrupole (MQ and EQ) resonant conditions in Fig. 2(e,f). Nonlinear propagation in larger Si NPs is strongly affected by laser-induced free carriers, providing additional asymmetry to the density or temperature profiles. The corresponding temperature profiles for NPs of interest are plotted in Fig. 3, with indicated input inten-

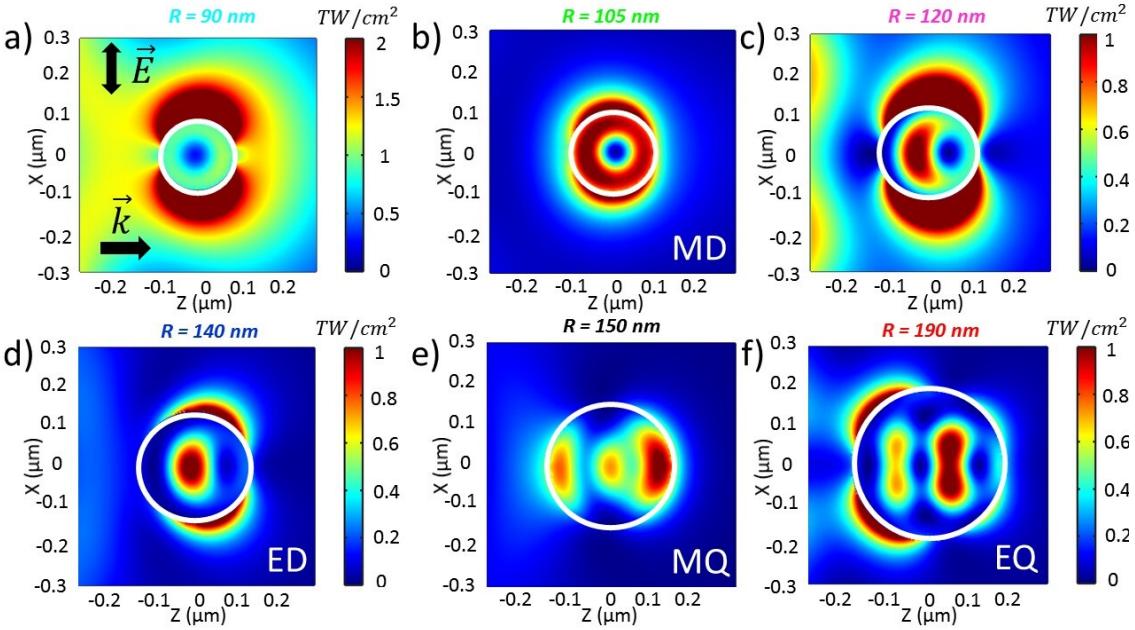

Figure 2: (a-f) Intensity distribution for NPs of radii (a) 90 nm, (b) 105 nm, (c) 120 nm, (d) 140 nm, (e) 150 nm, and (f) 190 nm at laser wavelength of $\lambda = 800$ nm. The input intensities I_0 for each sub-figure are chosen in order to reach the melting point for Si. White color circles mark the NP outlines, $\vec{k}$ shows the propagation direction and $\vec{E}$ indicates the linear polarization. Colorbar scale is the same for (b-f) but differs for (a).

sity values I_0. The smallest intensities of $I_0 \approx 65$ GW/cm^2 are required to reach locally the melting threshold inside the NP supporting MD resonance. In contrast, only the intensities of ≈ 20 times higher may cause damage in off-resonant NPs. In both cases, the maximum carriers reach $\approx 10^{21}$ cm^{-3}. One may expect that toroidal distributions of carriers covering larger volumes inside the NP would result in a stronger integrated harmonic signal. In contrast, the distributions with a pronounced hot spot enhance the interface effects and the field components providing second-order surface contributions. Additionally, the asymmetry of field and electron-hole plasma distributions affect the transmitted second-order harmonic.

In what follows, we define the efficiencies of SHG and THG as the ratio between the intensity signal at the harmonic of interest and the input intensity at the fundamental wavelength $\eta_{HG} = I_{HG}/I_0$. In order to separate the nonlinear effects induced by laser-induced carriers, we perform simulations with and without ionization processes. We calculate the temporal dynamics of each transmitted electric field component at the distance of λ from the center of the NP. Then, we perform separate Fourier Transforms for each component and sum up the contributions to get the intensity I_{HG} and normalized harmonic efficiency η_{HG}.

The results for SHG conversion efficiency for the NPs of interest are plotted in Fig. 4(a,b) with and without carriers respectively. The best performance occurs for NP supporting the ED resonance at $R = 140$ nm, whereas the NPs with MD resonance, having the strongest linear extinction cross-section in Fig. 1, transmit only slightly stronger harmonics comparing to the off-resonant cases. This tendency for the normalized efficiency is due to the fact that the absorption induced by free carriers and the yield of second harmonic have similar scaling respective to the electric field. Limiting the maximum absorption by the material damage threshold results in normalization of the harmonic signals. Nevertheless, the surface effects contribute stronger in case of ED resonance. Nonlinear propagation effects only slightly effect the second-order harmonic yield, with a resonance splitting effect pronounced only to the largest NP. However, we observe very strong saturation of the second-order harmonic efficiency with increasing incident field in Fig. 4(c), which occurs well below the material damage threshold.

The results for THG are shown in Fig. 4(d,e) with and without carriers respectively, indicating that the harmonic yield is enhanced by one order of magnitude by laser-induced carriers. The NPs supporting MD and MQ show the best performance for THG conversion efficiency, followed by ED and exceeding

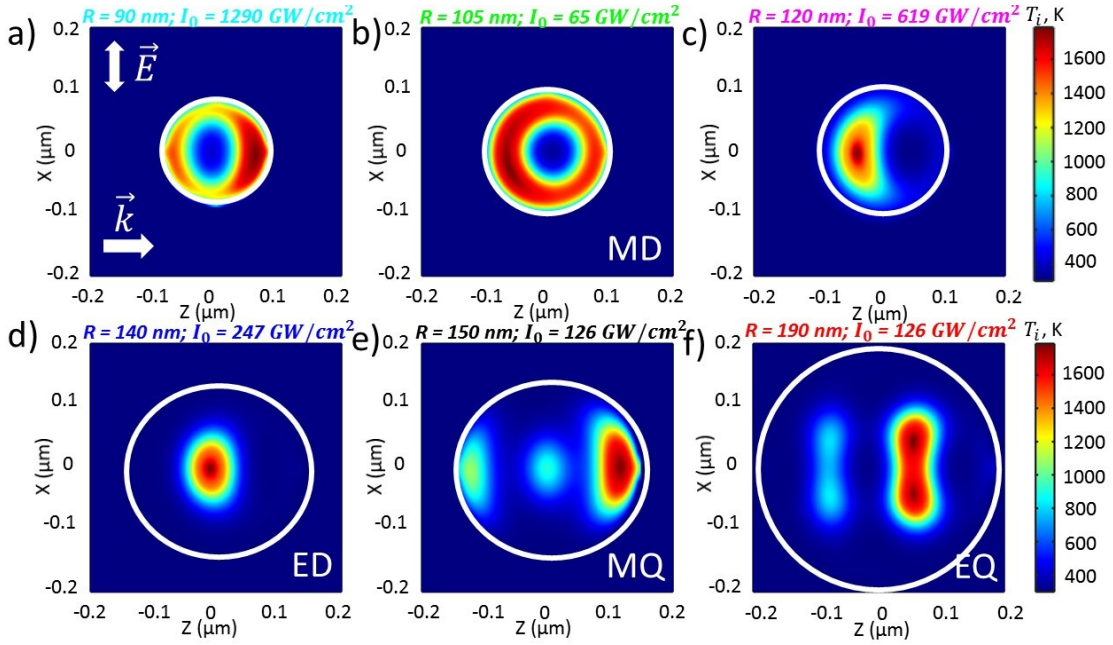

Figure 3: (a-f) Lattice temperature distribution in single NPs of radii (a) 90 nm, (b) 105 nm, (c) 120 nm, (d) 140 nm, (e) 150 nm, and (f) 190 nm at laser wavelength of $\lambda = 800$ nm. The input intensities I_0 required to reach the melting point for Si ($T_m = 1685$ K) are indicated in the upper part of sub-figures. White color circles mark the NP outlines, $\vec{k}$ shows the propagation direction and $\vec{E}$ indicates the linear polarization. Colorbar scale is the same for (a-f).

the efficiency in off-resonant case ($R = 90$ nm) by one order of magnitude. Interestingly, the performance without carriers scales with the corresponding extinction cross-sections for NPs in Fig. 1, however, the ratio is modified by laser-excited free carriers. Nonlinear propagation effects are also pronounced in this regime. The bigger NPs ($R = 150$ nm and $R = 190$ nm) exhibit splitting of a single maximum into two separated maxima. The THG spectra in the presence of electron plasma are significantly broader, slightly blue-shifted to higher-order harmonics (lower wavelengths). The ratio between third and fundamental harmonic I_{THG}/I_0 plotted in Fig. 4(f) for different input fields and $R = 105$ nm NP indicates that saturation effects due to absorption come into play slightly below the point where the damage threshold is reached.

Different trends for SHG and THG efficiencies in Fig. 4(a-b, d-e) shown by simulations with and without carriers indicate fully perturbative nature of the second harmonic (only slight changes) and transition from perturbative to non-perturbative behavior for the third harmonic (significant changes). Without carriers (or with weak carriers), Kerr effect is mainly responsible for the third order signal. In the case of strong electric fields, the laser-induced plasma inside the nanoparticles becomes a dominant non-perturbative source for the generation of the third harmonic and the amplitude is enhanced almost by one order of magnitude.

The weights of different modes are modified by the presence of laser-induced carriers due to changes in optical properties of silicon (both real and imaginary parts). Our simulations indicate that the spectrum broadening due to laser-induced plasma affects the quality factor of the resonator. As a result, the ratio between the harmonic efficiencies produced by magnetic and electric dipole or quadrupole resonances is less pronounced than for the case without carriers in Fig. 4(d-e).

3.2 Periodic arrangement

Lattice resonances in NP arrays can provide significant field enhancement inside the NPs and additional parameter flexibility (i. e. lattice spacing tuning) to optimize the optical response and to benefit from the coupled electric and magnetic resonances [47]. Importantly, it was shown that the spectral positions of ED and MD can be tuned independently to certain wavelengths by adjusting NP periodicity in $x-$ and $y-$ directions in infinite array of Si NPs [47]. In our work, we fix the central wavelength to 800 nm

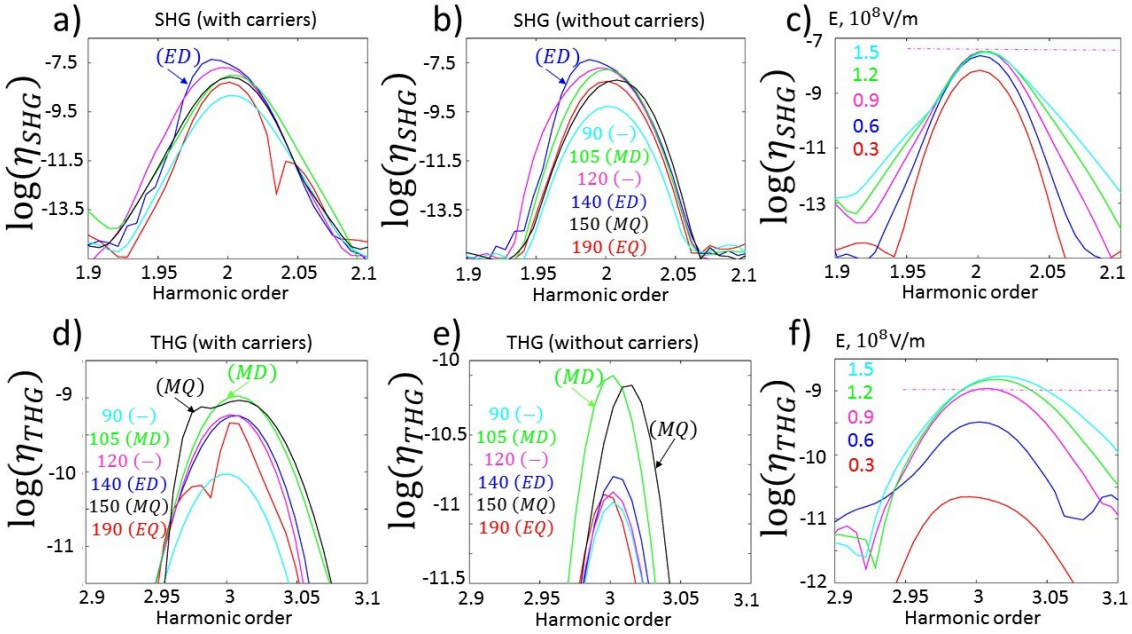

Figure 4: (a-b) SHG and (d-e) THG efficiency - simulations with and without free carriers for the NP radii of choice defined in (b, d, e) by different colors. (c) and (f) Saturation in SHG and THG growth for the applied electric fields indicated by different colors. The dashed line shows the threshold value where the melting point is achieved and the material damage is expected.

and perform optimization by varying both the NP radius in the relevant range and lattice spacings to achieve the strongest enhancement. This is done by applying an analytical model of resonant dipole-quadrupole coupling [48], successfully implemented for second harmonic generation in plasmonic periodic arrays [49] and validated for accuracy for both gold and Si nanosphere lattices around the lattice resonant position [50]. Here, we calculate the effective multipole polarizabilities and optimize the corresponding extinction cross-section for NPs in two-dimensional periodic array.

For instance, the intersection of ED and MD resonances corresponding to $R \approx 101$ nm and near-wavelength lattice spacings of $P_x = 760$ nm and $P_y = 790$ nm respectively exhibits a strong resonance at the 800 nm wavelength (see Fig. 5(a-c)). Under such conditions, a significantly lower input intensity would lead to strong field enhancement inside the particle and possible material damage. We perform nonlinear Maxwell simulations both for a single Si NP of $R = 101$ nm and for an infinite array of these Si NPs, introducing the periodic boundary conditions for the electric and magnetic fields at the borders of the FDTD domain, corresponding to the optimized lattice spacings in -x and -y directions. The threshold input intensity values of $\approx$ 34 GW/cm^2 are predicted for a NP array versus $\approx$ 181 GW/cm^2 for a single NP with the respective nonlinear intensity distributions shown in Fig. 5(d). Fourier Transforms of the corresponding transmitted field signals are compared in Fig. 5(f), indicating that even for few times lower input intensity, the harmonic yield is enhanced by two orders of magnitude both for second- and third-order harmonics. This result motivates further numerical and experimental studies exploiting resonant metasurfaces, supporting lattice resonances [47] or/and quasi-bound states in the continuum [4], in order to get the stronger harmonics with lower input energy below the material damage threshold.

The developed approach is expected to describe the nonlinear features of optical response including resonance splitting and blue shift, saturation in the harmonic yield and free carrier absorption in more advanced subwavelength systems, such as Mie-resonant periodic arrangements of nanodisks [1, 20], asymmetric metasurfaces supporting bound states in continuum and Fano resonances [2, 26, 31].

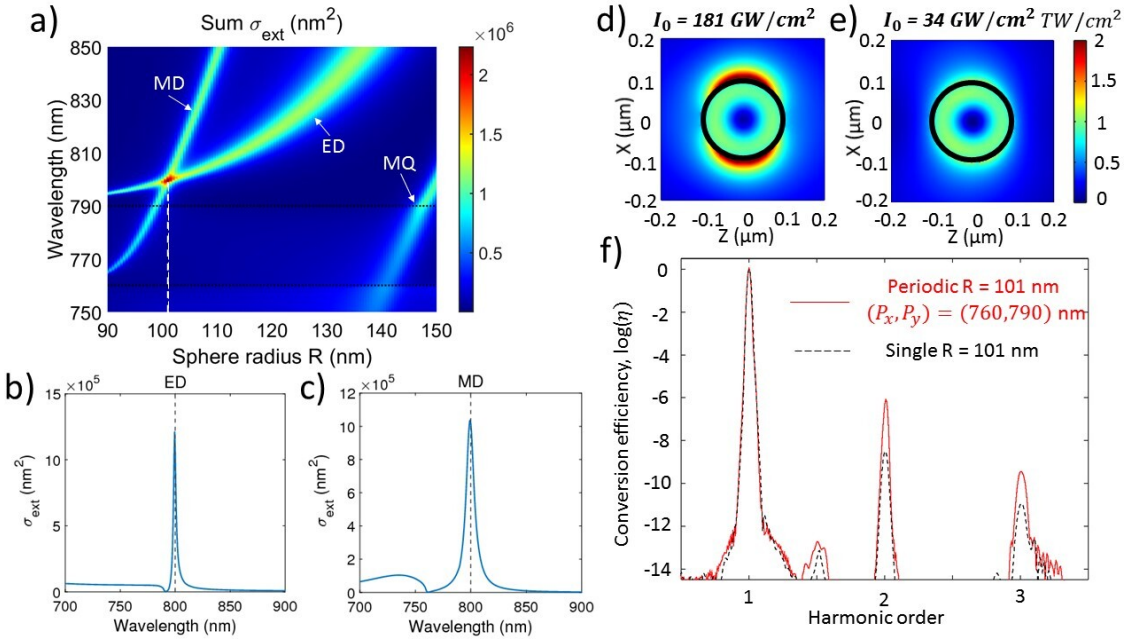

Figure 5: (a) Extinction cross-section as a function of laser wavelength and NP radius for (P_x, P_y)=(760, 790)nm lattice spacings (indicated by black dashed lines). (b,c) Electric (ED) and magnetic dipole (MD) resonances at 800 nm for a periodic infinite array of NPs with optimal R = 101 nm. (d,e) Intensity distributions in cases of a single NP (d) and NPs in periodic lattice (e). The input intensities I_0 to reach the melting thresholds for Si are indicated at the top of each subfigure. (f) Fourier transform of the transmitted field upon propagation through periodic lattice (red solid line) or a single NP (black dashed line).

4 Conclusions

In this work, we have addressed the limitations of second- and third-order harmonic conversion efficiencies in silicon nanoparticles, irradiated by femtosecond near-infrared laser pulses. In order to describe ultrafast dynamics involving the surface and bulk nonlinearities of a centrosymmetric semiconductor, free carrier absorption and material damage in a self-consistent way, we have developed a numerical model, coupling nonlinear Maxwell equations, electron-hole plasma kinetics and electron-ion transfer for silicon. We demonstrate that the nonlinear response of single nanoparticles can be altered by an order of magnitude beyond the aforementioned limitations, with the highest performance of nanoparticles supporting electric dipole resonance for the second harmonic and magnetic dipole and quadrupole for the third harmonic. Introducing a periodic array of nanoparticles and optimizing the inter-particle spacings to support both electric and magnetic dipole resonances, we were able to further enhance the nonlinear response by two orders of magnitude. Similar procedure can be applied to arbitrary geometries, different semiconductor materials and laser irradiation conditions, in order to design advanced active compact nanosources for efficient harmonic generation.

Acknowledgements
This work was supported by an Air Force Office for Scientific Research under awards no. FA9550-19-1-0032, FA9550-17-1-0246, and FA9550-21-1-0463.

Conflict of interest
The authors declare no conflict of interest.

References

[1] M. R. Shcherbakov, D. N. Neshev, B. Hopkins, A. S. Shorokhov, I. Staude, E. V. Melik-Gaykazyan, M. Decker, A. A. Ezhov, A. E. Miroshnichenko, I. Brener, et al., *Nano Letters* **2014**, *14*, 11 6488.

[2] Y. Yang, W. Wang, A. Boulesbaa, I. I. Kravchenko, D. P. Briggs, A. Puretzky, D. Geohegan, J. Valentine, *Nano Letters* **2015**, *15*, 11 7388.

[3] S. V. Makarov, M. I. Petrov, U. Zywietz, V. Milichko, D. Zuev, N. Lopanitsyna, A. Kuksin, I. Mukhin, G. Zograf, E. Ubyivovk, et al., *Nano Letters* **2017**, *17*, 5 3047.

[4] K. Koshelev, S. Kruk, E. Melik-Gaykazyan, J.-H. Choi, A. Bogdanov, H.-G. Park, Y. Kivshar, *Science* **2020**, *367*, 6475 288.

[5] G. Grinblat, *ACS Photonics* **2021**, *8*, 12 3406.

[6] V. Zubyuk, L. Carletti, M. Shcherbakov, S. Kruk, *APL Materials* **2021**, *9*, 6 060701.

[7] M. R. Shcherbakov, H. Zhang, M. Tripepi, G. Sartorello, N. Talisa, A. AlShafey, Z. Fan, J. Twardowski, L. A. Krivitsky, A. I. Kuznetsov, et al., *Nature Communications* **2021**, *12*, 1 1.

[8] G. Zograf, K. Koshelev, A. Zalogina, V. Korolev, R. Hollinger, D.-Y. Choi, M. Zuerch, C. Spielmann, B. Luther-Davies, D. Kartashov, et al., *ACS Photonics* **2022**, *9* 567.

[9] N. Bloembergen, R. K. Chang, S. Jha, C. Lee, *Physical Review* **1968**, *174*, 3 813.

[10] H. Tom, T. Heinz, Y. Shen, *Physical Review Letters* **1983**, *51*, 21.

[11] J. Sipe, D. Moss, H. Van Driel, *Physical Review B* **1987**, *35*, 3 1129.

[12] W. L. Mochán, J. A. Maytorena, B. S. Mendoza, V. L. Brudny, *Physical Review B* **2003**, *68*, 8 085318.

[13] Y. Zeng, W. Hoyer, J. Liu, S. W. Koch, J. V. Moloney, *Physical Review B* **2009**, *79*, 23 235109.

[14] M. Scalora, M. A. Vincenti, D. de Ceglia, N. Akozbek, V. Roppo, M. Bloemer, J. W. Haus, *Physical Review A* **2012**, *85*, 5 053809.

[15] C. Varin, R. Emms, G. Bart, T. Fennel, T. Brabec, *Computer Physics Communications* **2018**, *222* 70.

[16] K. Frizyuk, I. Volkovskaya, D. Smirnova, A. Poddubny, M. Petrov, *Physical Review B* **2019**, *99*, 7 075425.

[17] C. Reitböck, D. Stifter, A. Alejo-Molina, K. Hingerl, H. Hardhienata, *Journal of Optics* **2016**, *18*, 3 035501.

[18] M. Cazzanelli, J. Schilling, *Applied Physics Reviews* **2016**, *3*, 1 011104.

[19] D. Timbrell, J. W. You, Y. S. Kivshar, N. C. Panoiu, *Scientific Reports* **2018**, *8*, 1 1.

[20] M. R. Shcherbakov, P. P. Vabishchevich, A. S. Shorokhov, K. E. Chong, D.-Y. Choi, I. Staude, A. E. Miroshnichenko, D. N. Neshev, A. A. Fedyanin, Y. S. Kivshar, *Nano Letters* **2015**, *15*, 10 6985.

[21] S. Liu, M. B. Sinclair, S. Saravi, G. A. Keeler, Y. Yang, J. Reno, G. M. Peake, F. Setzpfandt, I. Staude, T. Pertsch, et al., *Nano Letters* **2016**, *16*, 9 5426.

[22] P. P. Vabishchevich, S. Liu, M. B. Sinclair, G. A. Keeler, G. M. Peake, I. Brener, *ACS Photonics* **2018**, *5*, 5 1685.

[23] V. V. Zubyuk, P. P. Vabishchevich, M. R. Shcherbakov, A. S. Shorokhov, A. N. Fedotova, S. Liu, G. Keeler, T. V. Dolgova, I. Staude, I. Brener, et al., *ACS Photonics* **2019**, *6*, 11 2797.

[24] A. Rudenko, K. Ladutenko, S. Makarov, T. E. Itina, *Advanced Optical Materials* **2018**, *6*, 7 1701153.

[25] M. Taghinejad, Z. Xu, K.-T. Lee, T. Lian, W. Cai, *Physical Review Letters* **2020**, *124*, 1 013901.

[26] H. Liu, C. Guo, G. Vampa, J. L. Zhang, T. Sarmiento, M. Xiao, P. H. Bucksbaum, J. Vučković, S. Fan, D. A. Reis, *Nature Physics* **2018**, *14*, 10 1006.

[27] A. Rudenko, M. K. Hagen, J. Hader, S. W. Koch, J. V. Moloney, *Photonics Research* **2022**, *10*, 9 2099.

[28] S. Makarov, S. Kudryashov, I. Mukhin, A. Mozharov, V. Milichko, A. Krasnok, P. Belov, *Nano Letters* **2015**, *15*, 9 6187.

[29] H. Cai, Q. Huang, X. Hu, Y. Liu, Z. Fu, Y. Zhao, H. He, Y. Lu, *Advanced Optical Materials* **2018**, *6*, 14 1800143.

[30] J. Xiang, J. Chen, Q. Dai, S. Tie, S. Lan, A. E. Miroshnichenko, *Physical Review Applied* **2020**, *13*, 1 014003.

[31] I. S. Sinev, K. Koshelev, Z. Liu, A. Rudenko, K. Ladutenko, A. Shcherbakov, Z. Sadrieva, M. Baranov, T. Itina, J. Liu, et al., *Nano Letters* **2021**, *21*, 20 8848.

[32] E. A. A. Pogna, M. Celebrano, A. Mazzanti, L. Ghirardini, L. Carletti, G. Marino, A. Schirato, D. Viola, P. Laporta, C. De Angelis, et al., *ACS Nano* **2021**, *15*, 7 11150.

[33] A. Taflove, S. C. Hagness, et al., *Norwood, 2nd Edition, MA: Artech House, l995* **1995**.

[34] A. Rudenko, J.-P. Colombier, T. E. Itina, *International Journal of Numerical Modelling: Electronic Networks, Devices and Fields* **2018**, *31*, 2 e2215.

[35] M. Falasconi, L. Andreani, A. Malvezzi, M. Patrini, V. Mulloni, L. Pavesi, *Surface Science* **2001**, *481*, 1-3 105.

[36] C. C. Wang, A. N. Duminski, *Phys. Rev. Lett.* **1968**, *20* 668.

[37] L. Rodríguez-Suné, J. Trull, M. Scalora, R. Vilaseca, C. Cojocaru, *Optics Express* **2019**, *27*, 18 26120.

[38] A. D. Bristow, N. Rotenberg, H. M. Van Driel, *Applied Physics Letters* **2007**, *90*, 19 191104.

[39] K. Sokolowski-Tinten, D. von der Linde, *Physical Review B* **2000**, *61*, 4 2643.

[40] A. Rämer, O. Osmani, B. Rethfeld, *Journal of Applied Physics* **2014**, *116*, 5 053508.

[41] H. M. van Driel, *Phys. Rev. B* **1987**, *35* 8166.

[42] E. J. Yoffa, *Phys. Rev. B* **1980**, *21* 2415.

[43] T. Sjodin, H. Petek, H.-L. Dai, *Phys. Rev. Lett.* **1998**, *81* 5664.

[44] G. Mie, *Annalen der Physik* **1908**, *330*, 3 377.

[45] A. Assadillayev, T. Hinamoto, M. Fujii, H. Sugimoto, S. Raza, *Nanophotonics* **2021**, *10*, 16 4161.

[46] P. Lorazo, L. J. Lewis, M. Meunier, *Physical Review B* **2006**, *73*, 13 134108.

[47] V. E. Babicheva, A. B. Evlyukhin, *Laser & Photonics Reviews* **2017**, *11*, 6 1700132.

[48] V. E. Babicheva, A. B. Evlyukhin, *Physical Review B* **2019**, *99*, 19 195444.

[49] A. Han, C. Dineen, V. E. Babicheva, J. V. Moloney, *Nanophotonics* **2020**, *9*, 11 3545.

[50] A. Han, J. V. Moloney, V. E. Babicheva, *The Journal of Chemical Physics* **2022**, *156*, 11 114104.

Table of Contents

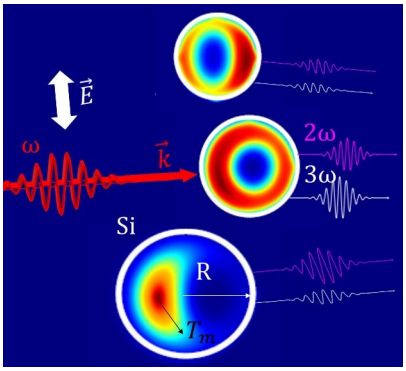

Second- and third-order harmonics can be efficiently generated in silicon nanoparticles by femtosecond laser irradiation. Free carrier absorption and material damage, however, may appear as the limiting factors upon intense excitation. An original approach coupling the aforementioned phenomena is applied to solve the trade-off problem for individual nanoparticles supporting different types of Mie resonances and their periodic arrays.